# Accepted Manuscript


Experimental and numerical investigation of blade–tower interaction noise

Branko Zajamsek, Yendrew Yauwenas, Con J. Doolan, Kristy L. Hansen, Victoria Timchenko, John Reizes, Colin H. Hansen

PII: S0022-460X(18)30812-5

DOI: https://doi.org/10.1016/j.jsv.2018.11.048

Reference: YJSVI 14531

To appear in: *Journal of Sound and Vibration*

Received Date: 21 May 2018

Revised Date: 27 November 2018

Accepted Date: 28 November 2018

Please cite this article as: B. Zajamsek, Y. Yauwenas, C.J. Doolan, K.L. Hansen, V. Timchenko, J. Reizes, C.H. Hansen, Experimental and numerical investigation of blade–tower interaction noise, *Journal of Sound and Vibration* (2019), doi: https://doi.org/10.1016/j.jsv.2018.11.048.

# Experimental and numerical investigation of blade–tower interaction noise

Branko Zajamsek[a], Yendrew Yauwenas[b], Con J. Doolan[b], Kristy L. Hansen[a], Victoria, Timchenko[b], John, Reizes[b], Colin H. Hansen[c]

[a]*College of Science and Engineering, Flinders University, Adelaide 5042, Australia*
[b]*School of Mechanical and Manufacturing Engineering, University of New South Wales, Sydney 2052, Australia*
[c]*School of Mechanical Engineering, University of Adelaide, Adelaide 5005, Australia*

**Abstract**

This paper describes the generation of blade–tower interaction (BTI) noise from upwind turbines and pylon-mounted fans using a combination of experimental and numerical means. An experimental rotor-rig was used in an anechoic chamber to obtain BTI acoustic data under controlled conditions. A computational model, based on the solution of the unsteady Reynolds Averaged Navier Stokes (URANS) equations and Curle's acoustic analogy, was used to describe the generation of fan and simplistic model of wind turbine BTI noise by the rotor-rig. For both the fan and model wind turbine case, the tower was found to be a more significant source of BTI noise than rotor blades. The acoustic waveforms for both turbine and fan are similar; however, in the case of the turbine, the blade contribution reinforces that from the tower, while in the case of a fan, there is some cancellation between the tower source and the blade source. This behavior can be explained by the unsteady aerodynamics occurring during BTI.

*Keywords:* Blade-tower interaction noise, Fluid-structure interaction,

Wind turbine noise, Fan noise

## 1. Introduction

Blade–tower interaction (BTI) noise is unsteady aerodynamic noise due to the aerodynamic interaction between rotor blades and a tower. In more general terms, the interference can be between blades and an arbitrary object (a tower, counter-rotating propeller or pylon for example) obstructing the flow upwind or downwind of the rotor. Because the blades interfere with an object periodically for a short amount of time the resulting noise is periodic and has an impulsive character. This is an important noise source, as it can be of major importance for various rotating systems ranging from helicopter rotors to modern upwind wind turbines. For the case of upwind wind turbines, it has been recently demonstrated that BTI noise can have an effect (mainly via providing increased background noise) on measurement systems used for detecting seismic activity and nuclear explosions [1, 2]. BTI also creates impulsive torque changes, which may contribute to a reduction in the fatigue life of the gearbox [3]. Detailed knowledge about this noise source generating mechanism is thus warranted to inform BTI noise control and mitigation strategies.

BTI noise is generated by the change in loading on the blades and tower. The change in loading is due to two aerodynamic phenomena working simultaneously, namely; 1) a reduced inflow velocity field upwind of the tower and 2) blade-passage effects. The principle of the change in loading as the blade passes through the reduced velocity field upwind of the tower is shown in Fig. 1a. The reduced velocity field upwind of the tower exists because the

tower is a significant obstruction in the flow, causing the wind to slow down before passing it. This reduced velocity field causes a change in the angle of attack on the passing blade and the rate of change of that angle of attack is a source of BTI noise [4]. Blade-passage effects results from the interaction between the aerodynamic disturbance generated by the blades and the tower, as also shown in Fig. 1a and in more detail in Fig. 1b, using the example of a helicopter rotor passing close to the tail boom. The aerodynamic disturbance describes the effect by which air is displaced by the moving blade as it passes the tower [6]. The air adjacent to the blade displaces outwards in a radial manner at the leading edge and converges in the wake of the trailing edge. This phenomenon has been numerically and experimentally demonstrated by Yauwenas *et al.* [6] on an unloaded (the blades pitch angle was 0°) three bladed rotor-rig. Yauwenas *et al.* [6] findings agree with Leishman and Bi [7], in that large pressure pulses due to the passage of the blade were reported.

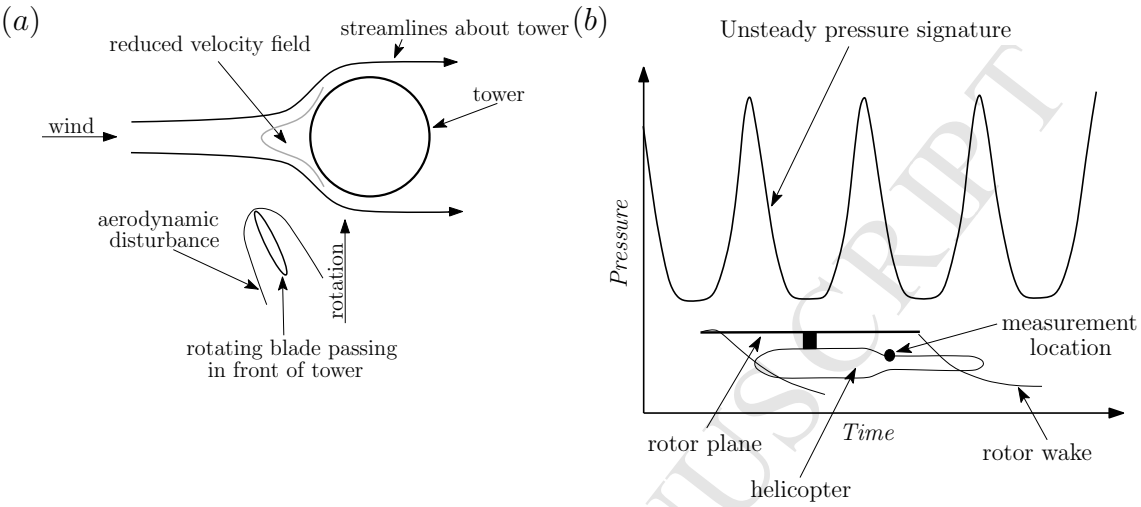


Figure 1: Schematic of blade–tower interaction (BTI). (a) Blade interaction with the reduced velocity field and blade-passage effects. (b) Unsteady pressure signature on the airframe below the helicopter rotor due to the blade-passage effects.

In the past, strong BTI noise has been associated with downwind wind turbines as described in Hubbard and Shepherd [9], which provoked many public complaints [8]. The high noise level was mainly the result of a large velocity deficit downwind of the tower and tower–blade vortex interaction, which produced strong pressure pulses occurring at the blade–pass frequency (BPF) [8, 9]. It was Greene [10] who showed experimentally on a scaled model of a wind turbine that changing the design to one with an upwind mounted rotor, one would significantly reduce the magnitude of the BTI noise. This is because the velocity deficit upwind of the tower is smaller than in the downwind direction and because there is no vortex shedding upwind of the tower. Greene's findings have been confirmed by Kelley [11] who performed measurements on a full scale upwind turbine and compared the results to earlier results obtained on a downwind turbine [8]. Apart from the research

on wind turbines, experimental studies have also been conducted on a rotor with downstream pylons [12] and on a helicopter tail boom by Leishman and Bi [7], both showing the creation of impulsive noise when the blade passes the pylon or tail boom.

Doolan *et al.* [13] proposed a first order aerodynamic model and the use of potential flow theory to explain an aerodynamic origin of BTI noise from modern upwind wind turbines. These authors then used the theory of Curle [4] to show that the far–field acoustic pressure due to blade–tower aerodynamic interaction results in pressure pulses at the blade–pass frequency. A similar method was employed by Madsen [14], who used blade element momentum theory and also assumed potential flow around the tower to approximate the forces generated on the turbine blades. The resulting noise was obtained by using the NASA-LeRC code [15]. Both studies omitted the non-linear interaction between the tower and blades. Furthermore, noise calculations considered only the force fluctuations on the blades, overlooking the fluctuations on the tower. Work by Leishman and Bi [7], which shows strong pressure fluctuations on a helicopter tail boom due to the passing blade, suggests that it is not unreasonable to expect the tower of a wind turbine to be a source of BTI noise as well. In fact, Yauwenas *et al.* [6] showed that, for an unloaded rotor (that is, a rotor whose blades are set at a pitch angle of 0°), the tower is the dominant source of noise during BTI.

Other numerical studies have been performed using computational fluid dynamics (CFD) on wind turbines with an upwind rotor to investigate the effect of BTI. Hsu and Bazilevs [16] used the sliding mesh method to simulate the rotation of the blades and showed changes to the force acting on

the blades due to BTI. The force oscillation was attributed to BTI as it occurred at the blade–pass frequency. A similar effect was reported by Mo *et al.* [17], who utilized the sliding mesh method and detected fluctuations in power output at the blade–pass frequency. Other studies, such as that by Zahle *et al.* [18], used the dynamic overset grid method to simulate blade rotation and also managed to detect an interaction between the tower and the blades. Wang *et al.* [19] reported pressure changes within the blade swept area, further indicating the significance of pressure changes on the tower due to BTI.

While successful in capturing the BTI effects by employing the sliding mesh methods, the numerical studies described above do not provide insight into the noise production mechanism. On the other hand, Nelson [20] used CFD to predict wind turbine noise using a permeable integration surface implementation of the Ffowcs-Williams Hawkings acoustic analogy [21] but did not consider the tower as the source of BTI noise. BTI noise production on rotors operating as a turbine or fan thus remain unclear.

In summary, previous experimental and numerical studies have shown that blade-passage causes a change in loading on the blades and the tower. This transient change in loading causes BTI impulsive noise and in the case of an unloaded fan the tower has been shown to be the dominant contributor [6]. However, only a few studies have considered both the blades and the tower in BTI noise prediction in the cases of an aerodynamically loaded fan and a model wind turbine. This is presumably because the changes caused by the tower are unimportant for power extraction of a wind turbine, but the same cannot be said for noise generation [6, 7]. The purpose of this

paper is therefore to present new knowledge about the BTI noise generated by loaded blades and the tower separately. The results were obtained from acoustic measurements and numerical simulations performed on a rotor-rig operated as a fan and an idealised wind turbine. This paper is structured as follows: Section 2 presents the experimental and numerical methods; Section 3 presents the aerodynamic and acoustic data; and the paper is concluded in Section 4.

## 2. Methodology

### *2.1. Rotor-rig*

A three bladed rotor-rig, as shown in Fig. 2, was was used for experimental and numerical study of BTI noise.

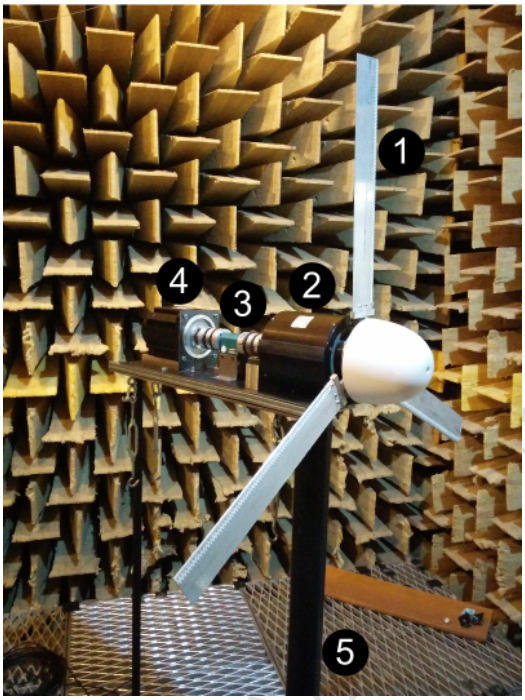


Figure 2: (Color online) Photograph showing the rotor-rig in the anechoic room. The rotor-rig parts are; 1) blades, 2) slip ring, 3) torque sensor, 4) 3 kW motor and 5) tower.

Figure 3 shows schematic diagram of the rotor-rig. The hub height of the rig was 1.42 m and the rotor plane diameter was 1.04 m. The blades were 450 mm long NACA 0012 airfoils with a constant 70 mm chord, 0° twist angle, and were mounted with 5° pitch angle, $\theta$. The blades were tripped at 10% of the chord length using 0.6 mm thick serrated tripping tape on both sides of the airfoil. The blade–tower distance, $d$, was set to 20 mm and 70 mm. The angular position of the blade is defined by an angle $\phi$, which is measured as shown in Fig. 3. This angle is 180° when the blade is aligned with the tower and is positive in the direction of the rotation. The rotor plane radius is marked by $R$ and is 520 mm. An arbitrary point in the rotor

plane is marked by position vector $r$. The rotor-rig was operated at constant 900 rotations per minute (RPM), which gives a blade–pass frequency of 45 Hz and blade tip speed of 49 $\text{ms}^{-1}$.

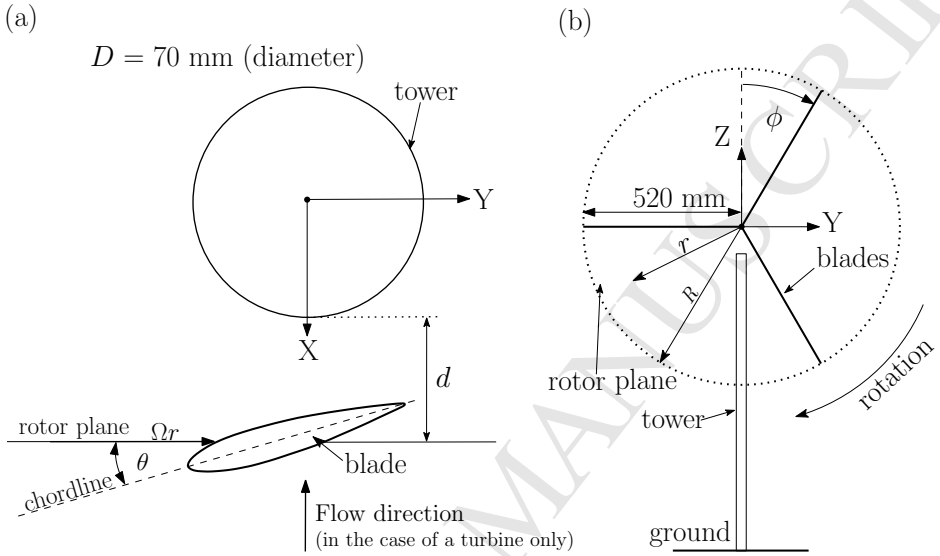


Figure 3: (a) shows definition of blade-tower distance $d$ and aerodynamic environment around the blade where $\theta$ is the pitch angle and $\Omega$ is the rotational frequency. (b) shows front view of the rotor-rig.

### *2.2. Laboratory measurements*

Acoustic measurement were done in the University of Adelaide's anechoic room, which has dimensions of 4.79 m × 3.9 m × 3.94 m (73.6 $\text{m}^3$) and provides a near–reflection free environment down to a frequency of ∼100 Hz. The acoustic data were recorded using a PXIe–4499 24–bit National Instrument data acquisition card and a B&K type 4955 1/2 inch microphone. The data were recorded for 60 seconds at a sampling rate of $2^{16}$ Hz. The acoustic time series were filtered using a 6th order Butterworth filter with a cut–off frequency at 1 kHz in order to remove undesirable noise.

The narrow-band power spectral density (PSD) estimation of experimental data was calculated using Welch's averaged modified periodogram method of spectral estimation using Hanning window, 50 percent overlap and 12 Hz frequency resolution. The simulated PSD was obtained in the same manner.

### *2.3. Computational model*

#### *2.3.1. Flow simulation*

Full details of the computational model can be found in Yauwenas *et al.* [6]. A summary and unique details concerned with this study are presented below. Due to the low Mach number based on the blade tip speed, the flow was assumed to be incompressible and governed by the following equations for continuity and momentum, respectively:

$$\frac{\partial u_i}{\partial x_i} = 0 \tag{1}$$

and

$$\rho\frac{\partial u_i}{\partial t} + \rho\frac{\partial}{\partial x_j}(u_i u_j) = -\frac{\partial p}{\partial x_i} + \frac{\partial \tau_{ij}}{\partial x_j}. \tag{2}$$

The stress tensor, $\tau_{ij}$, is related to strain rate by:

$$\tau_{ij} = (\mu + \mu_T)(\frac{\partial u_i}{\partial x_j} + \frac{\partial u_j}{\partial x_i}) \tag{3}$$

Since the flow is likely to be turbulent and the time step used in the numerical solution is relatively large, an SST $k$–$\omega$ turbulence model was used [22]. With the use of this model, a turbulent boundary layer around the blade was assumed, since blades on a rotor-rig were tripped as explained in Section 2.1. Equations 1 and 2 were solved using the finite volume solver

ANSYS FLUENT 14.5. The pressure–velocity coupling was done using the SIMPLEC method [23].

The timestep in the simulations was chosen to be 0.185 ms, which gives 1° rotation per timestep and a Nyquist frequency of 2.7 kHz. The convergence criteria at each timestep were set at a scaled residual of $10^{-4}$ for the continuity Eq. 1 and each directional component of the velocity. Convergence was typically attained in less than 30 iterations per timestep. Simulations were run for a total of 5040 time steps,which equals 14 complete rotor revolutions. Computations were performed on the Leonardi High Performance Computing cluster at the University of New South Wales, consisting of 48 AMD Opteron 6174 2.20 GHz processor cores with 128 GB of physical memory.

*2.3.2. Computational grid*

In order to capture the interaction between the blades and the tower, the sliding mesh method was employed [24]. In this method the spatial domain was split into two parts: one stationary and one rotating. These two parts were then coupled through a sliding interface. The rotating part contained the blades while the tower was in the stationary domain. This allows an accurate re-creation of the physics of the rotating mechanism and has already been successfully implemented in a study of wind turbines by Mo *et al.* [17].

The computational mesh used in this study has $11 \times 10^6$ elements. This was chosen as a result of a mesh refinement study. The grid is generally unstructured, except on the surfaces of the tower and the blades in order to allow more efficient post–processing. An inflation layer was generated around each blade to accurately capture the boundary layer effects. The maximum

$y^+$ value at the tip of the blade is around 5 and is lower for blade sections closer to the axis of rotation due to the lower velocity relative to the blade. The maximum aspect ratio of the cells in inflation layer around the airfoil is 25. There are at least 30 cells between the blade and the tower when $\phi = 180°$.

*2.3.3. Computational test cases*

Simulations were performed on two aerodynamically different test cases; namely fan and model wind turbine. In the simulation of the fan, no incoming wind was introduced into the rotor plane. This test case is identical to the experiment and serves as validation of the method, as well as understanding BTI of pylon mounted fans. As the computational model replicates the rotor-rig described in Section 2.1, it should be noted that the geometry is simplified (constant blade chord length, zero blade twist) and the Reynolds number based on chord length is much lower ($Re = 246,000$ at the tip of the blade) in comparison to an industrial wind turbine.

The model wind turbine test case is identical to that of the fan configuration in terms of computational grid and rotational speed (900 RPM), but with an incoming flow at 8.45 m/s, corresponding to a tip speed ratio $X_{TSR}$ of 5.8 ($X_{TSR} = \frac{v_{tip}}{V_\infty}$, where $v_{tip}$ is the blade tip speed and $V_\infty$ is the inflow speed). This value of $X_{TSR}$ was chosen because the theoretical point of maximum power extraction is expected to occur around that value [7].

*2.3.4. Far-field acoustics*

Using the flow simulation data, the far–field acoustic pressure was calculated using the compact formulation of an acoustic analogy introduced by

Curle [4]:

$$p'(t) = \frac{1}{4\pi c_0}\frac{s_i}{s^2}\frac{\partial}{\partial t}[F_i(t)], \tag{4}$$

where $c_0$ is speed of sound, $s$ is the distance between the source and the observer, $F(t)$ in the force on the surfaces of the blades and the tower, and the subscript $i = X, Y, Z$ indicates the directional component, as illustrated in Fig. 4. The far-field observer is positioned on the axis of rotation at 1.4 m away from the blade rotation plane. Because the observer is positioned less than one acoustic wavelength from the source for frequencies below approximately 240 Hz, the level of near–field contamination was assessed by adding a dipole source term to the right-hand side of Eq. 4 [5]. In this manner the near–field contribution was found to increase the acoustic pressure root mean square by 0.3% relative to the far–field contribution only. Hence, only the far–field term was used when implementing Curle's analogy. This is the only observer position considered in this work at which there is zero translational motion between the blades and the observer. From this it follows that the relative Mach number between the blades and the observer is also zero and thus the rigid body assumption used in deriving the compact formulation of Curle's analogy holds true. However, it should be noted that this assumption is not valid when the observer moves away from the axis of rotation. When assuming a characteristic length of $l = 3D$, the compact approximation is valid for a frequency range up to 1214 Hz or the 26th harmonic number. The characteristic length is based on the observation of the tower surface pressure field height in the $Z$ direction in Fig. 8. A more detailed description of the method is provided in Yauwenas *et al.* [6].

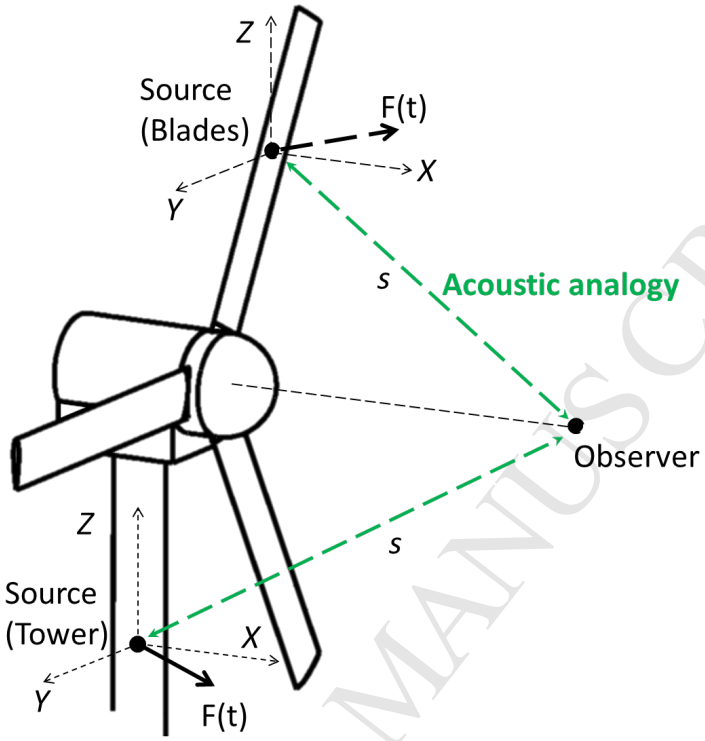


Figure 4: Schematic diagram of the source and the observer in Curle's acoustic analogy.

## 3. Results

### *3.1. Rotor-rig aerodynamics*

#### *3.1.1. Overall flow environment*

Figures 5a and b show the computed flow structure around the rotor-rig for the fan and model wind turbine configuration, respectively. The flow structure is visualised using the lambda–2 criterion, which identifies the vortex core in an incompressible flow by taking the eigenvalues of $S^2+\Omega^2$, where $S$ and $\Omega$ are the symmetric and asymmetric part of the velocity gradient tensor [26], respectively. Figure 5 shows the isosurface of the second eigenvalue

$\lambda_2 = -1000$ s$^{-2}$ in terms of its magnitude.

For both configurations in Fig. 5, the tip vortices produced by the blades are evident. The tip vortex core of the preceding blade does not directly impinge the following blade as they are carried downstream by the induced flow in the case of the fan and by the incoming flow in the case of model wind turbine. At the blade span close to the axis of rotation ($r/R \sim 0.5$), a series of vortices is present for the model wind turbine configuration. These vortices can be attributed to stall phenomena occurring due to the high effective angle of attack at the blade span positions close to the hub.

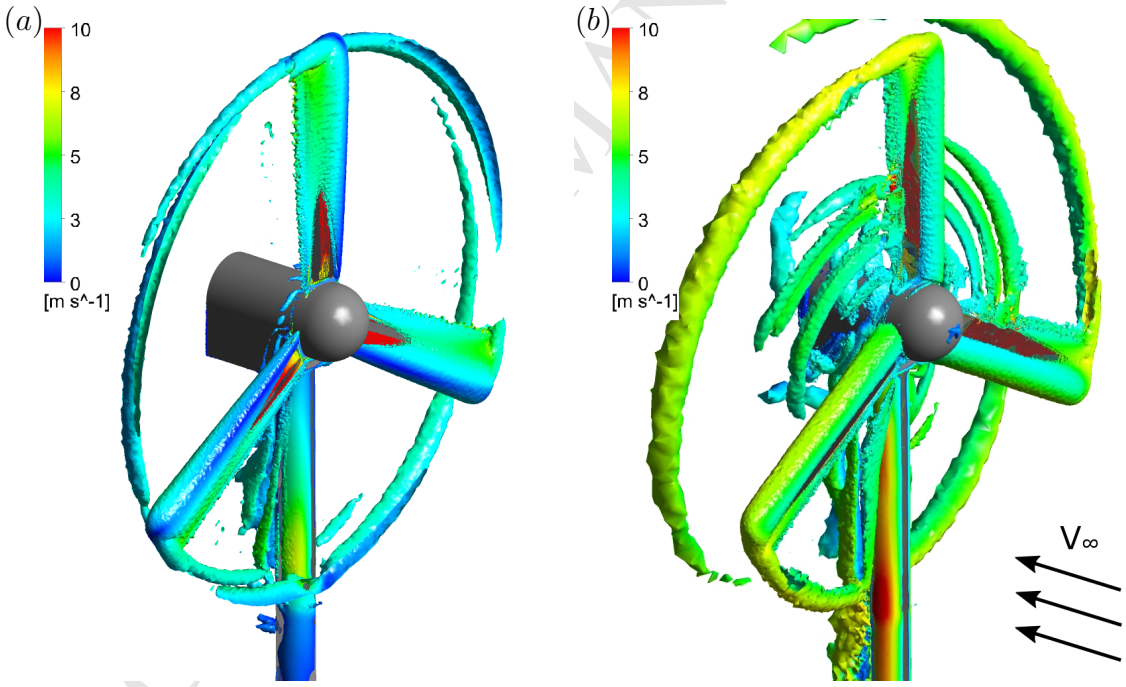


Figure 5: Flow structure visualisation using the lambda–2 criterion (isosurface of $\lambda_2 = -1000$ s$^{-2}$) around the rotor-rig for (a) the fan and (b) the model wind turbine configuration at $\theta = 5°$ and 900 RPM. The isosurface is coloured by the velocity component in the X-direction.

The NACA0012 airfoil is expected to stall at $\alpha > 10°$ for the Reynolds number based on the velocity at the mid-span of the blade which yields $Re = 1.16 \times 10^5$ [27]. Figure 6 shows the effective angle of attack along the span of the blade in the absence of BTI effect, for the cases of fan and model wind turbine with $\theta = 5°$. This figure suggests that the stall will occur along the portion of the blade span $r/R < 0.65$ and $X_{TSR}$ of 5.8.

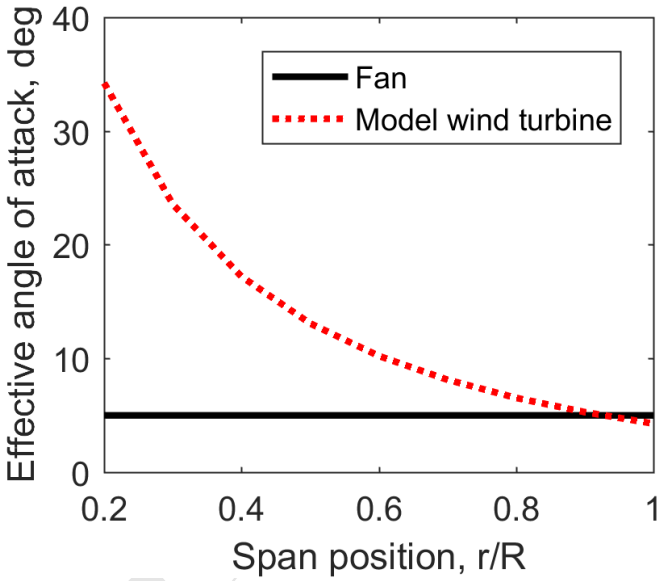


Figure 6: Effective angle of attack along the blade span with $\theta = 5°$ for both the fan (a) and the model wind turbine (b) configurations, and $X_{TSR} = 5.8$ for the model wind turbine configuration.

*3.1.2. Pressure field*

In Fig. 7, the computed pressure field on the plane at -$Z/R = 0.8$ (below the axis of rotation) during the BTI for fan and model wind turbine configurations, is shown. The pressure field is shown at three blade azimuthal positions during the blade-passage, namely, $\phi = 170°$, $180°$ and $190°$. As

can be seen in Fig. 7, a typical pressure distribution around the airfoil contains high–pressure regions at the leading and trailing edge. The difference between a turbine and a fan is that in the case of a turbine, the suction side of the airfoil faces the tower and in the case of a fan, the suction side faces away from the tower. This difference in suction side orientation for the fan and turbine can be seen in Fig. 7.

When a blade is approaching the tower at $\phi = 170°$ in both the fan and turbine cases, the leading edge high pressure region interacts with the tower, as shown in Figs. 7a and b. A similar interaction between a blade and the tower in both cases can be observed when the blade has just passed the tower and is positioned at $\phi = 190°$. In the latter blade angular position, the trailing edge high pressure region, generated by the sink, affects the tower. When the blade is aligned with the tower at $\phi = 180°$, the low pressure region (suction side of a blade) interacts with the tower in the case of the model wind turbine, as shown in Figs. 7b, d and f. Comparing the two cases, the interaction at $\phi = 180°$ is stronger for the turbine case, since the suction side of a blade on a fan is facing away from the tower and its pressure side, which interacts with the tower, is weak.

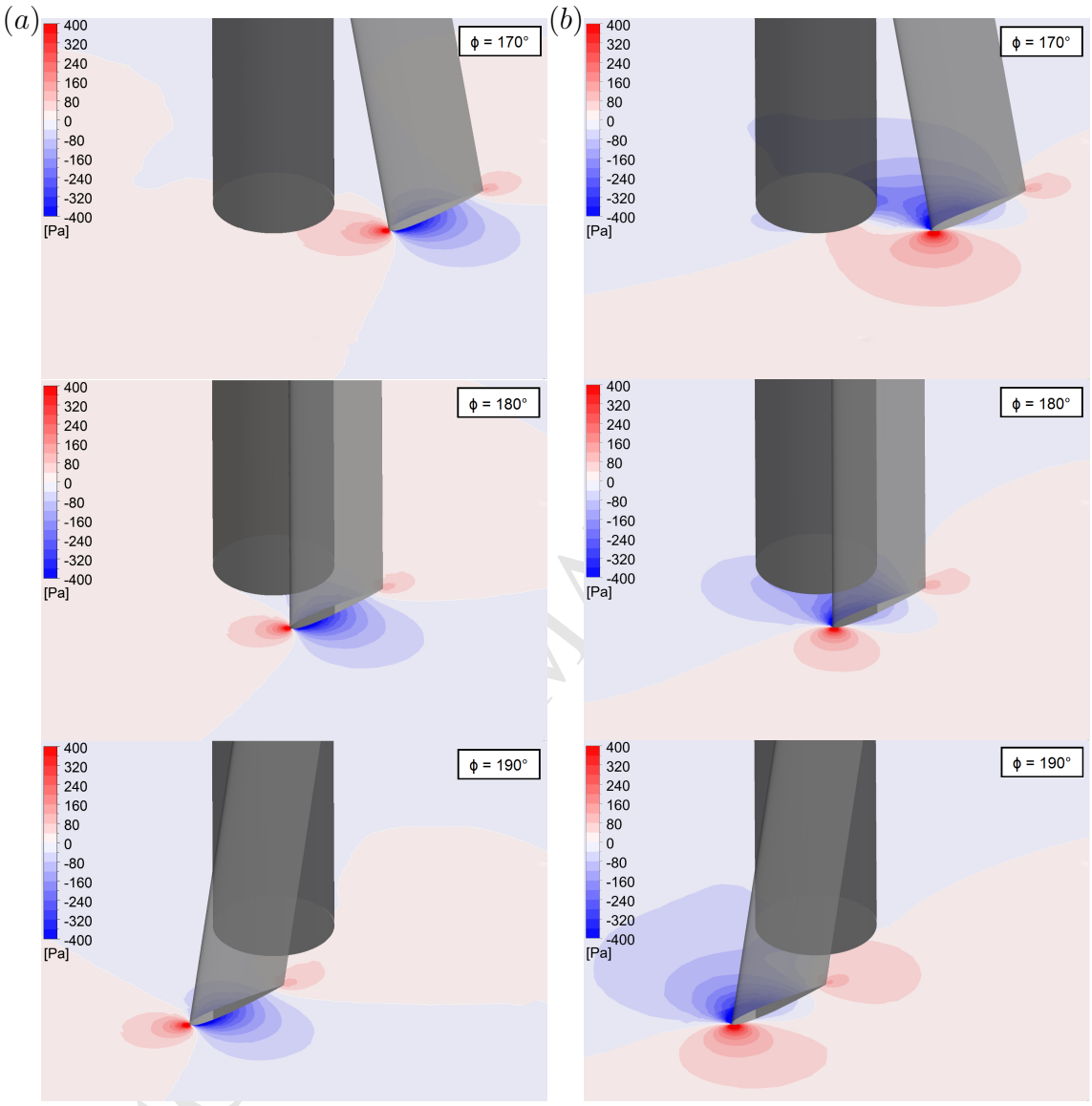


Figure 7: (Color online) Pressure field in the plane $-Z/R = 0.8$ during BTI ($\phi = 170°$, 180° and 190°) for ($a$) the fan and ($b$) the model wind turbine configurations at $\theta = 5°$ and 900 RPM.

Complementary to Fig. 7, surface pressure distributions on the surface of the tower during BTI for the fan and model wind turbine configurations is

shown in Fig. 8. In the case of the fan in Figs. 8 a, c and e, the blade–tower pressure interaction is more prominent towards the tip of the blade due to a higher induced velocity in that region. The induced velocity is estimated to be $\approx 4$ ms$^{-1}$ at $Z/R \approx 0.85$. For more details see Fischer *et al.*[33] who investigated the velocity field produced by this rotor-rig by comparing numerical simulations with experimental data. The pressure magnitude reaches its peak at -$Z/R \sim 0.8$ (best evident in Fig. 8c) and falls rapidly beyond that point, due to the pressure leakage over the blade tip [28]. For the model wind turbine configuration, the blade tip vortex appears to have an influence on the pressure field, since the maximum pressure is observed to occur above the blade radius, as best evident in Fig. 8f. This is due to the presence of the oncoming wind convecting the tip vortex in the downstream direction towards the tower, as may also be observed from the tip vortex visualisation in Fig. 5b. Furthermore, the model wind turbine tip vortex is stronger in comparison to the fan due to the increased lift generation and hence it is reasonable to expect its contribution to the tower surface pressure filed is greater as well.

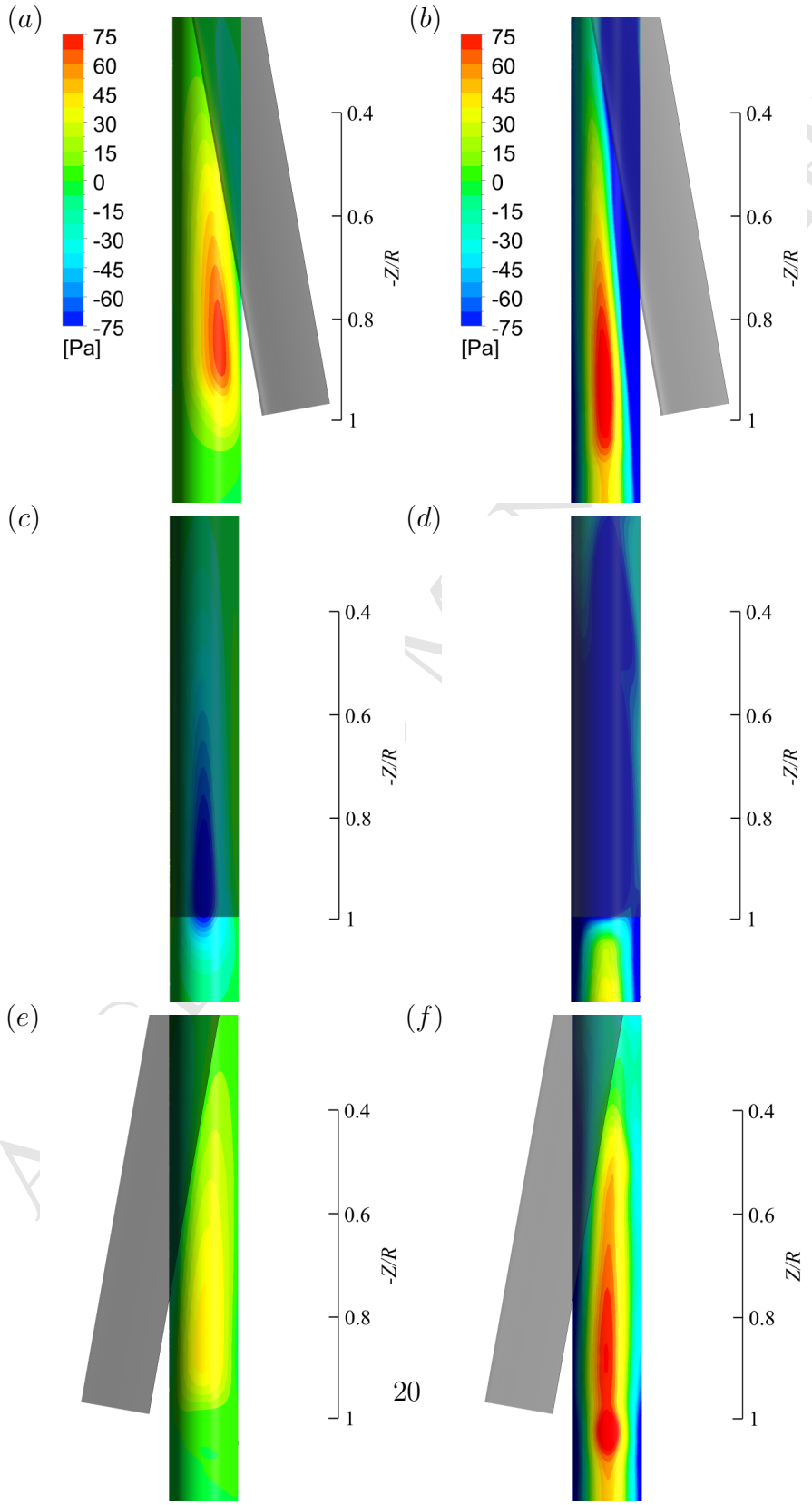


Figure 8: Pressure field on the upwind surface of the tower during BTI at various blade angular positions, $\phi$; ($a$, $b$) $\phi = 170°$, ($c$, $d$) $\phi = 180°$ and ($e$, $f$) $\phi = 190°$. Fan cases are shown on the left ($a$, $c$, $e$) and the model wind turbine cases on the right ($b$, $d$, $f$).

*3.1.3. Unsteady thrust*

Thrust is defined as a force parallel to the axis of rotation, which is positive in $-X$ direction and is presented here because the far-field acoustic pressure is directly related to the forces acting on the blades via Curle's acoustic analogy [4]. The thrust coefficient, $C_T$, is defined as $\frac{T}{0.5\rho v_{tip}^2 A}$, where $T$ is the thrust on a single blade or a tower, $\rho$ is the density of air, $v_{tip}$ is the blade tip speed and $A$ is the planform area of a single blade.

Figure 9 shows a time history of the thrust coefficient acting on a blade over one rotation of the rotor, for both the fan and the model wind turbine configuration. For clarity, the results are shown for a single blade only as all blades experience the same thrust (shifted by $2\pi/3$ rad). A pulse is observed occurring when a blade passes over the tower. When a blade is not interacting with the tower, the $C_T$ is constant at approximately -0.052 and 0.23 for the fan and the model wind turbine, respectively. These constant $C_T$ values are determined by the effective angle of attack, which is different for the fan and the turbine configuration. For the fan case shown in Fig. 9a, the negative $C_T$ pulse indicate a temporary increase of thrust acting on the blade away from the tower due to blade-passage effects. This is because the pressure side of a blade interacts with the tower when $\phi \sim 180°$ (see Fig. 7a). In contrast, the BTI results in a temporary reduction of the thrust acting on a blade in the case of the model wind turbine shown in Fig. 9b. This reduction is caused by a blade passing through the region of velocity deficit immediately upwind of the tower, decreasing the strength of flow circulation around a blade. The transient increase after the $C_T$ peak minima is due to the change in effective angle of attack as the oncoming wind has to navigate around the tower.

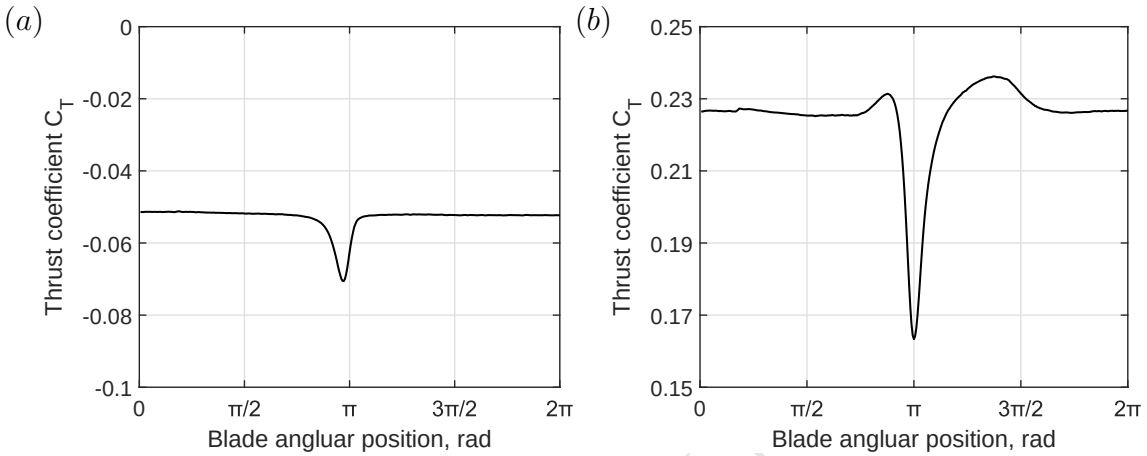


Figure 9: Simulated thrust coefficient, $C_T$, on a blade over one rotation for ($a$) the fan ($b$) the model wind turbine configuration at $\theta = 5°$ and 900 RPM. The thrust coefficient range is 0.1 on both figures for ease of comparison.

This is confirmed by inspecting the variation in the effective angle of attack at $r/R = 0.8$ as the blade passes the flow region modified by the presence of the tower, shown in Fig. 10. The analytical solution was computed assuming potential flow around the tower for the model wind turbine configuration with $d/D = 2/7$ and 1. Analogous to the $C_T$ fluctuations in Fig. 9, there is a significant decrease in effective angle of attack when $\phi = 180°$, which is accompanied by a small increase in effective angle of attack immediately before and after passing the tower.

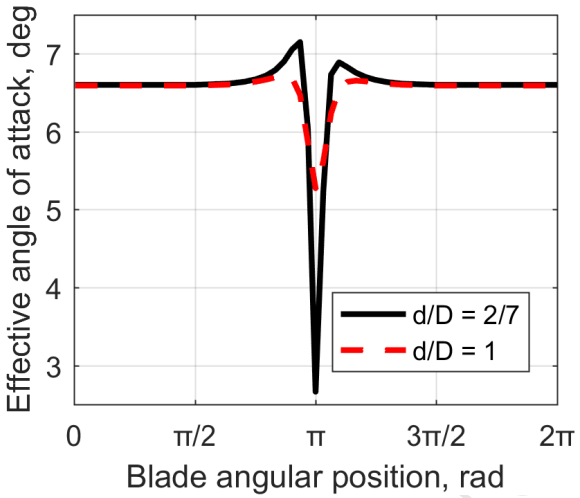


Figure 10: Effective angle of attack during BTI on a single blade at $r/R = 0.8$ for the model wind turbine configuration obtained from analytical solution.

In Fig. 11 the time history of thrust coefficient acting on the tower for both configurations is shown. In the case of the fan shown in Fig. 11a, the thrust pulses on the tower are relatively more complex than those acting on the blade shown in Fig. 9a. There are additional local maxima observed just before and right after the minimum point of $C_T$. This suggests that the changes on the tower during BTI are due to blade-passage effects, where high pressure regions around the leading and trailing edge of the passing blade interact with the tower. As may be seen in Fig. 11b, the local maximum prior to the main peak is much weaker for the model wind turbine configuration. This is because the suction side of the blade is facing towards the tower, which causes the portion of the tower surface directly downwind of the blade to experience a significant pressure decrease, as can be seen in Fig. 8b. This low-pressure region negates the increase of $C_T$ on the tower due to the pressure

increase caused by the high-pressure region ahead of the leading-edge of the blade.

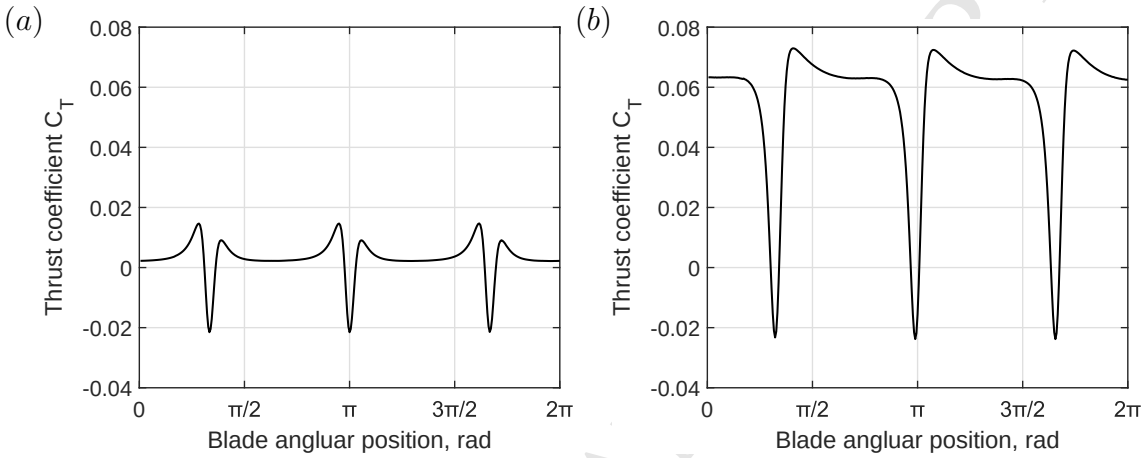


Figure 11: Simulated thrust coefficient on the tower over one blade rotation for ($a$) the fan ($b$) the model wind turbine configuration at $\theta = 5°$ and 900 RPM.

### *3.2. Rotor-rig acoustics*

#### *3.2.1. Fan configuration*

Figure 12 shows that BTI noise produces only low frequency tonal noise since the broadband spectra at higher frequencies ($> 700$ Hz) is similar for both blade-tower separation distances. The broadband noise predominantly consists of trailing edge noise as shown by Zajamsek *et al.*[32].

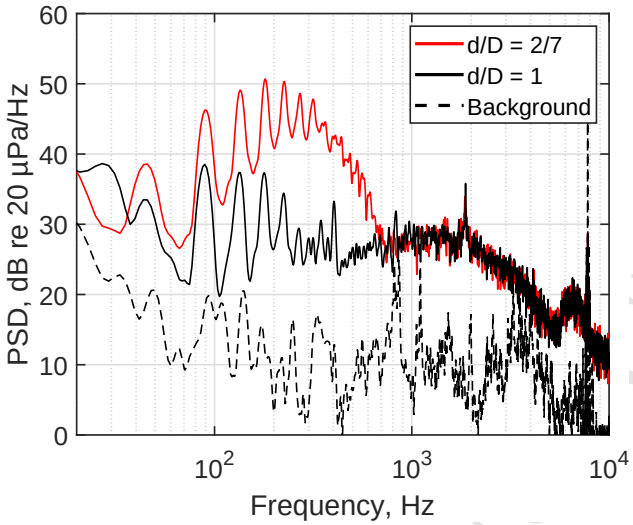


Figure 12: Experimental power spectral density of a fan at 900 RPM, $\theta = 5°$ and two blade-tower separation distances.

In Fig. 13, experimental and numerical ensemble averaged acoustic pressure waveforms and corresponding power spectral densities for the fan configuration, are shown. The acoustic pressure was measured on the axis of rotation as shown in Fig. 3 at 1.4 m from the rotor plane. For the experimental results, the ensemble acoustic pressure averages were computed over 50 seconds and thus comprise approximately 750 rotor revolutions, whereas for the simulation results there were computed over 4 rotor revolutions. Such a small number of simulated revolutions is deemed to be sufficient for removing small perturbations due to the high consistency between each revolution waveform. In Fig. 13, three pressure pulses per revolution due to BTI, are observed in experimental and simulated waveforms for both separation distances. Time domain pulses transform into a tonal components in the frequency domain that occur at the blade pass frequency and harmonics, as shown in Fig. 13c

and d. Here, simulated and experimental power spectrum density spectra are in reasonable agreement at the blade pass frequency (45 Hz) and harmonics. While the BTI noise can be best observed in Fig. 13a, the separation distance of one tower diameter is more realistic in the context of an industrial wind turbine [14, 3]. A discrepancy between the peak simulated and measured pulse values is noticeable and is most likely due to experimental uncertainties (errors in blade pitch angle and blade-tower distance), presence of extraneous noise sources and numerical errors and limitations of the assumptions used in the formulation of the acoustic analogy. This discrepancy is particularly evident in Fig. 12b due to the low BTI noise signal magnitude and hence lower signal-to-noise ratio. Variations between the peak amplitudes of BTI pressure pulses are attributed to the small differences between each blade's weight and mounting conditions in the experiments. These differences are also considered small for the discrepancies between measure and simulated spectra. However, the BTI noise signal trends are similar for both separation distances which indicates a similar BTI noise production mechanism at both blade-tower distances.

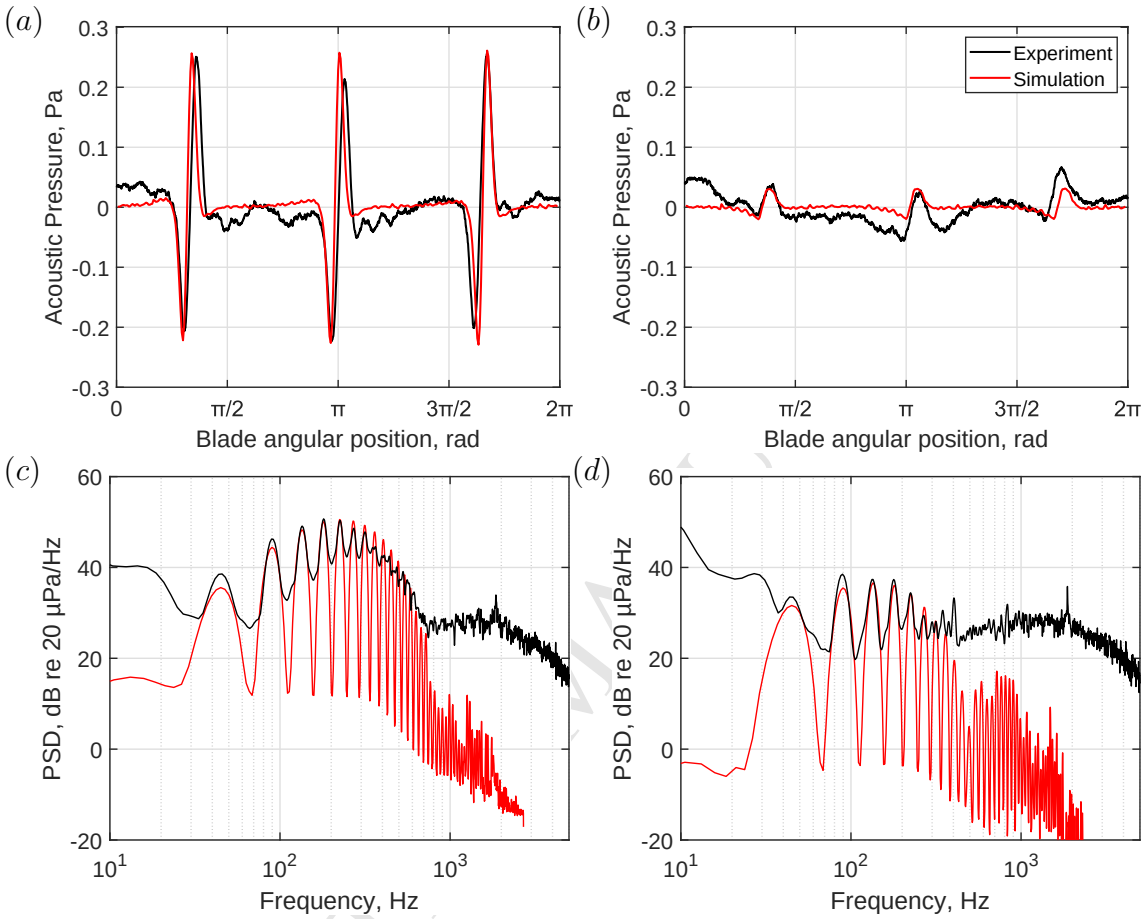


Figure 13: Measured and simulated ensemble averaged acoustic pressure waveforms and power spectral densities for the fan configuration at (a, c) $d/D = 2/7$ and (b, d) $d/D = 1$.

Figure 14 presents the simulated ensemble acoustic pressure waveforms due to BTI for the fan configuration, along with the separate contributions from the tower and the blades. Similar to the findings presented in Yauwenas *et al.* [6], the contribution from the tower is significantly higher than that from the blades, with the peak magnitude being about twice as high. According to the definition of the thrust coefficient, $C_T$, directly related to the far-field

acoustic pressure, the difference between the blades and the tower acoustic emissions is predominantly due to the difference in thrust and not difference in surface areas. Although the overall amplitude of the waveform is lower for $d/D = 1$ shown in Fig. 14b, the importance of the tower contribution relative to the blade is consistent for both blade-tower distances. These observations reveal that BTI noise is not solely generated by the blades as has been previously assumed [13, 29]. The resulting waveform over one blade-pass is characterised by two major peaks; one minima immediately followed by a maxima. These two major peaks are attributed to a large transient change in surface pressure as acoustic pressure generation is directly related to the rate of change of the surface pressure on the blades and the tower. Clearly seen are also two minor peaks, one preceding and one following the maxima/minima major peaks. The minor peaks are attributed to the high pressure regions around the leading and trailing edge interacting with the tower. The leading and trailing edge high pressure regions and their interaction with the tower can be seen in Fig. 7.

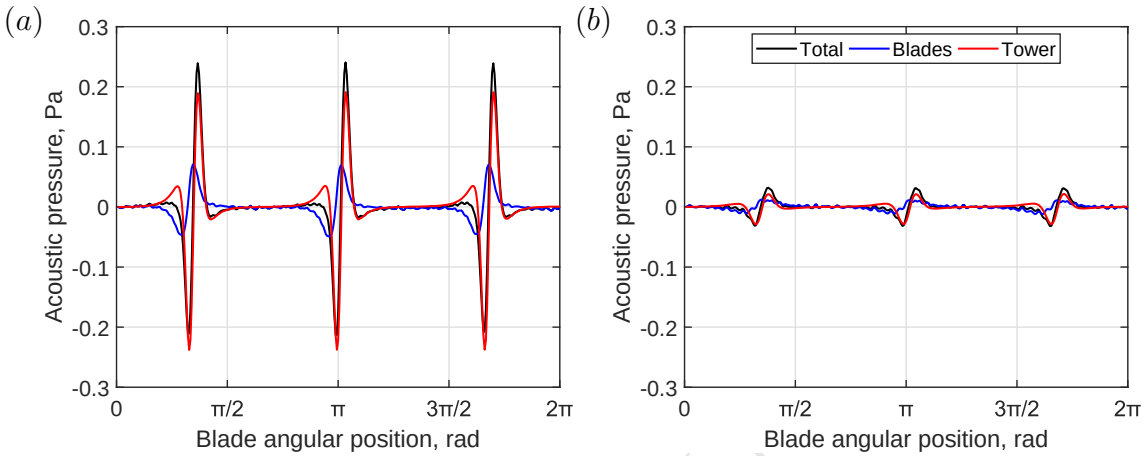


Figure 14: Simulated ensemble averaged acoustic pressure waveforms for the fan configuration at (a) $d/D = 2/7$ and (b) $d/D = 1$.

### *3.2.2. Model wind turbine configuration*

Figure 15a and c shows simulated ensemble averaged acoustic pressure waveforms in terms of blade, tower and total contribution, for the rotor-rig operating as a model wind turbine. A similar waveform pattern is observed for both blade-tower separation distances with $d/D = 1$ yielding lower magnitude in comparison to $d/D = 2/7$. Unlike the fan configuration, the waveform consists of only two major peaks without any minor peaks being observed in the vicinity of the major peaks. For the model wind turbine configuration, the dominant BTI noise production mechanism acting on a blade is a blade passing through a region of velocity deficit immediately upwind of the tower which temporary reduces the thrust force acting on a blade as shown in Fig. 11b. This reasoning is reconfirmed by the similarity of the simulated acoustic waveform in Fig. 15a ("total") with the simulated waveform made by Doolan *et al.* [13], who assumed BTI to be solely caused by the blades

passing the velocity deficit region upwind of the tower.

By comparing the BTI noise production mechanisms of the fan and model wind turbine configurations, a few similarities and differences are apparent. Fan acoustic pressure peaks due to the blades and the tower are slightly out-of-phase (blade pressure pulses precedes tower pressure pulses) meaning that the drop in thrust during BTI occurs earlier on the blades than the tower. This is not apparent in the case of the model wind turbine where the drop in thrust on blades and the tower happen simultaneously. When considering only the blades, the BTI noise production mechanism for the fan configuration is dominated by blade-passage effects (that is the flow field generated by the rotating blades which is modified by the tower), while for the turbine configuration the dominant BTI noise production mechanism is the blade passing the velocity field upwind of the tower consisting of reduced inflow velocity field and blade-passage effects. Although the mechanisms of BTI noise production by the blade for the fan and turbine configurations are different, the mechanism affecting the tower in both configurations is dominated by blade-passage effects. As is the case for the fan configuration, the tower is also found to be the dominant BTI noise source for the model wind turbine configurations at both $d/D = 2/7$ and 1.

As can be seen in Fig. 15b and d, the BTI produces a tonal spectrum centered at the blade pass frequency and upper harmonics. The spectra for $d/D = 1$ contains fewer upper harmonics in comparison to $d/D = 2/7$ which is expected since the BTI pulses in the time domain are visibly sharper for $d/D = 2/7$ in comparison to $d/D = 1$. For both separation distances, the contribution from the tower is dominant and increases with frequency. Such

a spectral shape in the infrasonic frequency region is commonly observed in the vicinity of modern industrial wind turbines [31, 1] with its hypothesized origin to be the blade tower interaction [1]. Due to the simplistic design of the model wind turbine case in the current simulations (as discussed in Section 2.3.4), the observations regarding the BTI noise generating mechanism cannot be extrapolated to an industrial wind turbine. But as the results of these simulations are revealing, similar simulations on an industrial wind turbine are warranted.

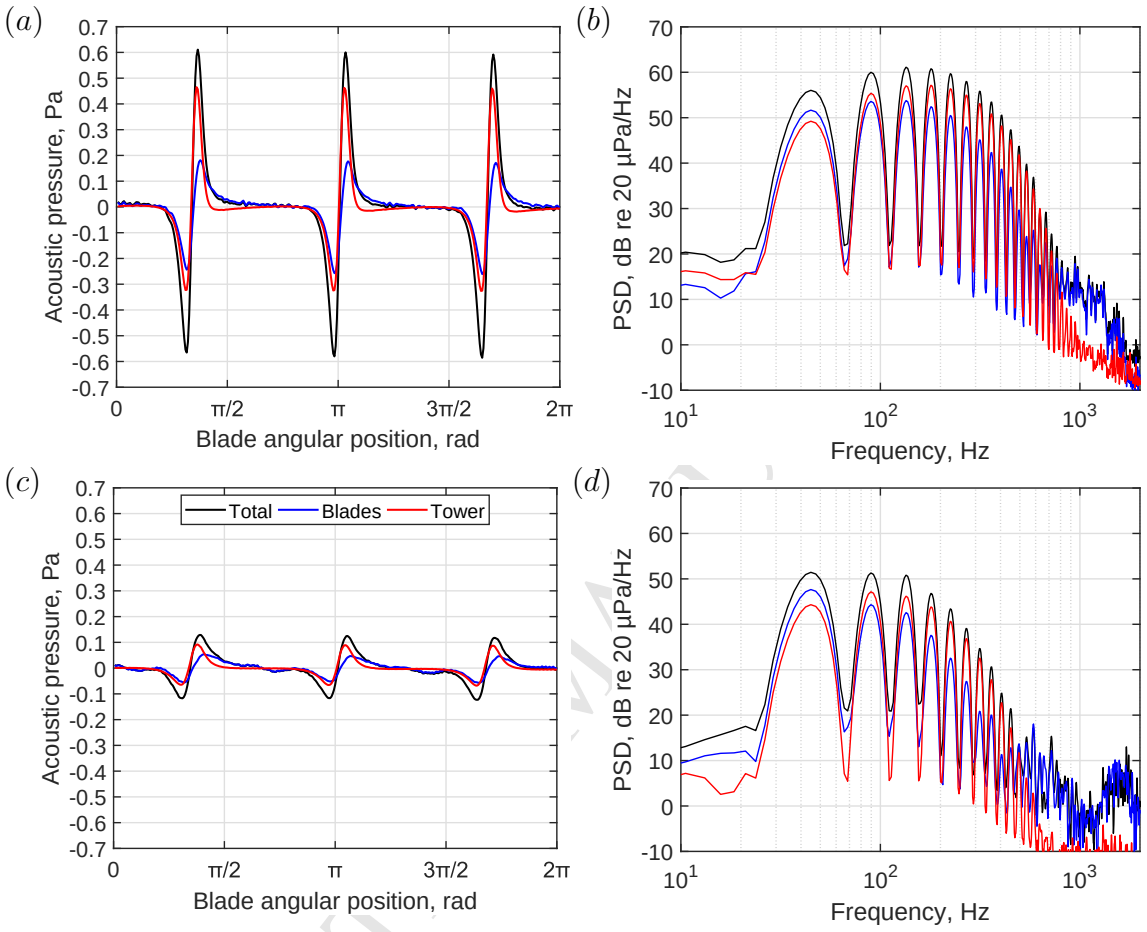


Figure 15: Simulated acoustic emissions of a model wind turbine. (a) and (c) show simulated ensemble averaged acoustic pressure waveforms for $d/D = 2/7$ and 1, respectively. (b) and (d) show power spectral density for $d/D = 2/7$ and 1, respectively.

## 4. Conclusions

When rotating blades encounter aerodynamic disturbances due to the presence of a support tower or pylon, an impulsive blade–tower interaction (BTI) noise is emitted as a result. In the case of an upwind wind turbine, the tower interaction with the incoming flow creates a reduced velocity field

in front of the tower, which together with blade-passage effects, forms such an aerodynamic disturbance. However, the precise role of the blades and tower in such a BTI noise generating mechanism are unknown. Here, it was numerically shown that the tower is the dominant noise source, which emits approximately twice as much noise as the blades. Previously, the role of the tower in BTI noise production was neglected. The results presented here thus open a new perspective on BTI noise generation by loaded blades, and consequently, on BTI noise control. Aerodynamic treatment of the tower (such as appropriately shaped fairings) might have a greater effect on reducing BTI noise in comparison with blade treatment only. Aerodynamic treatment of the tower will possibly reduce the impulsive torque on the gearbox, extending the life of the turbine. However, these conclusions are based on the numerical results obtained from a simplistic model of a wind turbine and hence more realistic simulations are warranted.

## 5. Acknowledgements

Financial support from the Australian Research Council, Project DP120102185 and DP130103136, is gratefully acknowledged.

## References

[1] C. Pilger and L. Ceranna, "*The influence of periodic wind turbine noise on infrasound array measurements*", J. Sound Vib. **388**, 188–200 (2017).

[2] K. Stammler, and L. Ceranna, "*Influence of Wind Turbines on Seismic Records of the Grafenberg Array*", Seismological Research Letters **87**(5), 1075–1081 (2016).

[3] F. Zahle and N. Sorensen, "*Overset grid flow simulation on a modern wind turbine*", *in 26th AIAA Applied Aerodynamics Conference*, Honolulu, Hawaii (2008).

[4] N. Curle, "*The influence of solid boundaries upon aerodynamic sound*", Proc. R. Soc. London A **231**, 505 – 514 (1955).

[5] Ann P. Dowling and John E.Ffowcs- Williams, *Sound and Sources of Sound* (Ellis Horwood, 1983), page XX

[6] Y. Yauwenas, B. Zajamsek, J. Reizes, V. Timchenko and C. J. Doolan, "*Numerical simulation of blade–passage noise*", J. Acoust. Soc. Am. **142**(3) 1575–1586 (2017).

[7] J. Leishman and N. Bi, "*Aerodynamic interactions between a rotor and a fuselage in forward flight*", J. Am. Helicopter Soc. **35**(3) 22 – 31 (1990).

[8] N. D. Kelley, H. McKenna, R. Hemphill, C. Etter, R. Garrelts and N. Linn, "*Acoustic noise associated with the MOD-1 wind turbine: its source, impact, and control*", Technical Report by Solar Energy Research Institute (1985), pp. 262.

[9] H. H. Hubbard and K. P. Shepherd, "*Aeroacoustics of large wind turbines*", J. Acoust. Soc. Am. **89**(6) 2495–2508 (1991).

[10] C. G. Greene, "*Measured and calculated charateristics of wind turbine noise*", Report, No. CP 2185, National Aeronautics and Space Administration (1981), pp. 355 – 362.

[11] N. D. Kelley, H. McKenna, E. Jacobs, R. Hemphill and N. Birkenheuer, "*The MOD-2 wind turbine: Aeroacoustical noise sources, emissions, and potential impact*", Report No. TR – 3036, Solar Energy Research Institute (1988), pp. 212.

[12] T. Enoki, H. Kodama and S. Kusuda, "*Investigation of fan rotor interaction with pressure disturbance produced by downstream pylon*", *in ASME Turbo Expo 2013: Turbine Technical Conference and Exposition*, San Antonio, Texas (2013).

[13] C. Doolan, D. J. Moreau and L. A. Brooks, "*Wind turbine noise mechanisms and some concepts for its control*", Acoustics Australia **40**(1) 7 – 13 (2012).

[14] H. Madsen, "*Low frequency noise from wind turbines mechanisms of generation and its modelling*", J. Low Freq. Noise, Vib. Act. Control **29**(4) 239 – 251 (2010).

[15] G. Guidati, J. Ostertag, and S. Wagner, "*The NASA-LeRC wind turbine sound prediction code*", *in second DOE/NASA Wind Turbine Dyn. Workshop*, Cleveland, OH (1981), pp. 10.

[16] M.-C. Hsu and Y. Bazilevs, "*Fluid-structure interaction modeling of wind turbines: simulating the full machine*", Computational Mechanics **50**(6), 821 – 833 (2012).

[17] J.-O. Mo, A. Choudhry, M. Arjomandi and Y.-H. Lee, "*Large eddy simulation of the wind turbine wake characteristics in the numerical wind tunnel model*", J. Wind Eng. Ind. Aerodyn. **112**, 11 – 24 (2013).

[18] F. Zahle, N. N. Sorensen and J. Johansen, "*Wind turbine rotor-tower interaction using an incompressible overset grid method*", Wind Energy **12**(6), 594 – 619 (2009).

[19] Q. Wang, H. Zhou and D. Wan, "*Numerical simulation of wind turbine blade-tower interaction*", Journal of Marine Science and Application **11**(3), 321 – 327 (2012).

[20] C. C. Nelson, A. B. Cain, G. Raman, T. Chan, M. Saunders, J. Noble, R. Engeln, R. Dougherty, K. S. Brentner and P. J. Morris, "*Numerical studies of wind turbine acoustics*", *in 50th AIAA Aerospace Sciences Meeting including the New Horizons Forum and Aerospace Exposition*, Nashville, Tennessee (2012).

[21] K. S. Brentner and F. Farassat, "*Modeling aerodynamically generated sound of helicopter rotors*", Progr. Aerospace Sci. **39**(2), 83 – 120 (2003).

[22] F. R. Menter, "*Two-equation eddy-viscosity turbulence models for engineering applications*", AIAA J. **32**(8), 1598 – 1605 (1994).

[23] J. P. van Doormaal and G. D. Raithby, "*Enhancements of the SIMPLE method for predicting incompressible fluid flows*", Numer. Heat Transfer **7**(2), 147 – 163 (1984).

[24] "*ANSYS FLUENT 14.0 Theory Guide*" ANSYS, Inc. (2011).

[25] M. Hand, D. Simms, L. Fingersh, D. Jager, J. Cotrell, S. Schreck and S. Larwood, "*Unsteady aerodynamics experiment phase RN6: wind tunnel test configurations and available data campaigns*", Report No. NREL/TP-500-29955, National Renewable Energy Laboratory (2003).

[26] J. Jeong and F. Hussain, "*On the identification of a vortex*", J. Fluid Mech. **285** 69 – 94 (1995).

[27] E. Jacobs and A. Sherman, "*Airfoil Section Characteristics as Affected by Variations of the Reynolds Number*", NACA Technical Report 586, National Advisory Committee for Aeronautics (1937).

[28] I. H. Abbott and A. E. Von Doenhoff, "*Airfoil trailing edge noise measurements with a directional microphone*", *in 4th Aeroacoustics Conference*, Atlanta, USA (1977).

[29] G. P. van den Berg, "*The Beat is Getting Stronger: The Effect of Atmospheric Stability on Low Frequency Modulated Sound of Wind Turbines*", Journal of Low Frequency Noise, Vibration and Active Control **24**(1), 15 – 40 (2005).

[30] J. F. Manwell, J. G. McGowan and A. L. Rogers (), "*Wind energy explained: theory, design and application*", 2nd ed. (John Wiley & Sons, London)(2009).

[31] B. Zajamsek, K. L. Hansen, C. J. Doolan and C. H. Hansen, "*Characterisation of wind farm infrasound and low-frequency noise*", J. Sound Vib. **370**, 176–190 (2016).

[32] B. Zajamsek, C. Doolan, D. Moreau, J. Fischer and Z. Prime, "*Experimental investigation of trailing edge noise from stationary and rotating airfoils*", J. Acoust. Soc. Am. **141**(5) 3291–3301 (2017).

[33] J. R. Fischer, Y. Yauwenas, C.J. Doolan, V. Timchenko, J. Reizes, "*Unsteady Flow Physics of the Blade-Tower Interaction of a Pylon-Mounted*

*Fan*", *in 23rd AIAA/CEAS Aeroacoustics Conference*, Boulder, Colorado (2017).